Nanoscale

Accepted Manuscript

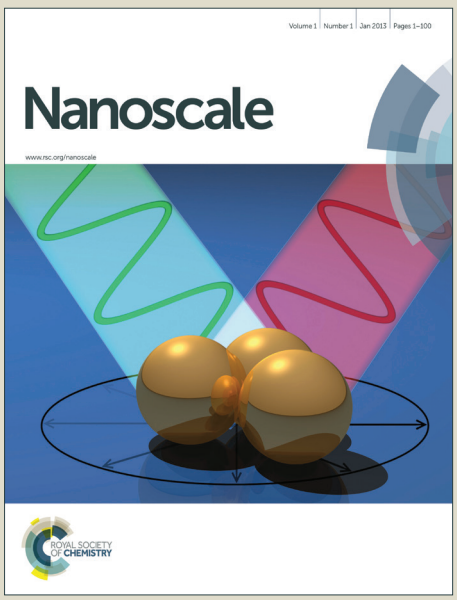

ROYAL SOCIETY OF CHEMISTRY

www.rsc.org/nanoscale

Nanoscale

Nanoscale

Dynamic Article Links ►

Cite this: DOI: 10.1039/c0xx00000x

www.rsc.org/nanoscale

PAPER

Selective on Site Separation and Detection of Molecules in Diluted Solution with Super-Hydrophobic Clusters of Plasmonic Nanoparticles†

Francesco Gentile,*[a,b] Maria Laura Coluccio,[b] Remo Proietti Zaccaria,[b] Marco Francardi,[c] Gheorghe Cojoc,[d] Gerardo Perozziello,[a] Raffaella Raimondo,[a] Patrizio Candeloro[a] and Enzo Di Fabrizio[c,a]

Received (in XXX, XXX) Xth XXXXXXXXX 20XX, Accepted Xth XXXXXXXXX 20XX
DOI: 10.1039/b000000x

Super-hydrophobic surfaces are bio-inspired interfaces with a superficial texture that, in its most common evolution, is formed by a periodic lattice of silicon micro-pillars. Similar surfaces reveal superior properties compared to conventional flat surfaces, including very low friction coefficients. In this work, we modified meso-porous silicon micro-pillars to incorporate networks of metal nano-particles into the porous matrix. In doing so, we obtained a multifunctional-hierarchical system in which (i) *at a larger micrometric scale*, the super-hydrophobic pillars bring the molecules dissolved in an ultralow-concentration droplet to the active sites of the device, (ii) *at an intermediate meso-scale*, the meso-porous silicon film adsorbs the low molecular weight content of the solution and, (iii) *at a smaller nanometric scale*, the aggregates of silver nano-particles would measure the target molecules with unprecedented sensitivity. In the results, we demonstrated how this scheme can be utilized to isolate and detect small molecules in a diluted solution in very low abundance ranges. The presented platform, coupled to Raman or other spectroscopies, is a realistic candidate for the protein expression profiling of biological fluids.

[a] BioNEM, University Magna Graecia of Catanzaro - Catanzaro, 88100, Italy. E-mail:gentile@unicz.it
[b] Istituto Italiano di Tecnologia, Via Morego, 30 16163 Genova, Italy
[c] King Abdullah University of Science and Technology, Thuwal 23955-6900, Kingdom of Saudi Arabia
[d] Max Planck Institute of Molecular Cell Biology and Genetics, Pfotenhauerstrasse 108, 01307 Dresden, Germany
† Electronic Supplementary Information (ESI) available: See DOI: 10.1039/b000000x/

Cite this: DOI: 10.1039/c0xx00000x

www.rsc.org/nanoscale

PAPER

1 Introduction

Super hydrophobic surfaces (SHSs) are bio-mimetic, artificial micro-fabricated interfaces, in which a pattern of cylindrical micro-pillars is modified to incorporate details at the nano-scale. For these systems, the integration of different scales translates into superior properties, including a vanishingly small friction coefficient. On account of this a fluid, on interacting with similar surfaces, would exhibit contact angles approaching, in some cases, 180° [1-3] (**Fig.1a-b**). The present, somehow impressive, notoriety of these surfaces[4-6] is due to a coincidence of factors that are: (i) the relatively simple and mathematically tractable models that describe the physics of small drops on a surface, (ii) the recent advances in materials science and nanotechnology whereby SHSs can be artificially reproduced, and (iii) the unmatched properties of such surfaces, whereby they can be utilized for a variety of very practical applications.

SHSs are typically fabricated using micro and nano fabrication techniques, on using which a two dimensional lattice is created by the repetition, or tessellation, of a regular pattern or motif. In doing so an artificial, periodic pattern is obtained, where the smallest unit of the pattern can be a silicon[2, 3, 7] or polymeric[8, 9] cylindrical micro pillar (**Fig.1c-d**). The upper surface of those pillars can be further modified to include a coating at the nano scales that may be, to name a few, a thin film of a polymeric organo-fluorine compounds as described in some papers of the group of Di Fabrizio [7, 10], or a nano-porous silicon matrix as in the work of Gentile al. [11]. In all cited examples, a two scale roughness is responsible for the non-wetting behaviour of the substrate[12-15], where the micro structure of the pillars and the nano structure of the covering combine to form surfaces that are clearly water repellent. In realizing those patterns, one should choose the correct ratio between the diameter and distance of the pillars, from which the solid fraction ϕ is determined. The choice is critical because, while small ϕ (that is, a sparse packing of pillars) will induce large contact angles, large ϕ (that is, a dense packing of pillars) would prevent the transition from the Cassie state[16], where the drop sits upon the pillars, to the Wenzel state[17], where instead the drops is pinned on the substrate [18-21].

An accurate fabrication of the surfaces can be realized on the basis of a criterion of rational design, as described in the paper of Gentile et al. [22], whereby the best trade-off between small and large ϕ can be determined.

The most practical property of SHSs is a reduced friction coefficient that yields a series of advantages. These advantages include, but are not restricted to[4], (i) the geometry and positioning of liquid droplets can be easily controlled; (ii) micro-patterns can be prefilled with aqueous solutions without the need for surfactants; (iii) droplets can be positioned extremely close to each other on a surface; (iv) super-hydrophobic regions in a Cassie-Baxter state can be used to create patterns to control bio-adhesion; and (iv) the discontinuous de-wetting effect arising from the extreme difference in contact angle hysteresis between the super-hydrophilic and super-hydrophobic regions can be used to passively dispense aqueous solution into the super-hydrophilic spots without wetting the super-hydrophobic background. Those advantages, in turn, may be exploited for applications spanning specific areas of the physical, engineering and biological sciences, sometimes bridging traditional disciplines. As for some examples, super-hydrophobic surfaces have been used for patterning complex geometries with liquids[23, 24], for separating oil and water[25], as an anti/bio-fouling coating[5, 26], for controlling the adhesion of proteins or bacteria on a surface[8, 27-29], for guiding the aggregation of primary neurons into three dimensional architectures[30], for imaging DNA fibers and gaining exclusive information of the double helix[31], for influencing cell adhesion and morphology and the production of the extra cellular matrix[32], in the very large area of cell microarrays technology[33].

Recently, a fistful of works demonstrated that similar surfaces may have a major impact in the field of biomedical devices and diagnostics. In the works of the group of Di Fabrizio [7, 10, 22], a family of hierarchical structures has been described with the ability of positioning and detecting a single molecule. These devices may be ultimately used for the *effective* early detection of cancers or the fast sequencing of genomes[34, 35].

In the scheme introduced in reference [7], a range of plasmonic structures was integrated into super hydrophobic silicon pillars. These metal structures serve as hot spots that intensify the local electric fields and consequently enhance the Raman signal by several orders of magnitude. Those devices function like a multistage system where, on a larger micrometric scale, the surface brings the molecules in an ultralow-concentration droplet to the active sites of the device where, on a smaller nanometric scale, nano-sensors would sense those molecules with unprecedented resolution. In the described system, the time scale of evaporation (ranging from few seconds to several minutes depending on the droplet size) is much smaller than the time scale of diffusion (ranging from hours to days), therefore, this mechanism *dramatically* shortens the time of flight of the target species to the photo-active sites of the device.[36, 37]

Noticeably, this scheme is *scalable* to obtain specific configurations or architectures. In a recent work, Lis and collegues[38] investigated the enhancement of the vibrational sum-frequency generation (SFG) signal from molecules adsorbed on metallic *nano-pillars* vertically aligned on a metallic surface. They demonstrated that in a similar system a largely improved sensitivity combines with spatial selectivity to boost the versatility of second-order vibrational SFG spectroscopy or microscopy, for applications as analytical molecular devices.

Here, this concept was developed even further. Using an innovative site selective electroless deposition method[39], clusters of metal nano-particles were introduced into a meso-porous

silicon matrix which, in turn, drapes an array of super-hydrophobic pillars (**Fig.1e-h**). The meso-porous silicon film has the function of adsorbing the low molecular weight content of a complex mixture, that can be then analyzed on account of the giant electromagnetic field, and Raman signal thereof, generated by the silver nano-particles ensemble.

In the described system, the clusters of metal nano-particles reveal a complex structure, with details over multiple scales. The cited structure is responsible for the local enhancement of the electromagnetic field by several order of magnitudes, that is not instead explicable using simpler linear geometries. A similar architecture may be instead reproduced introducing a diffusion limited aggregation model[40], where particles stick together to form an aggregate with a random fractal nature, with superior optical properties, as explained in the rest of the paper.

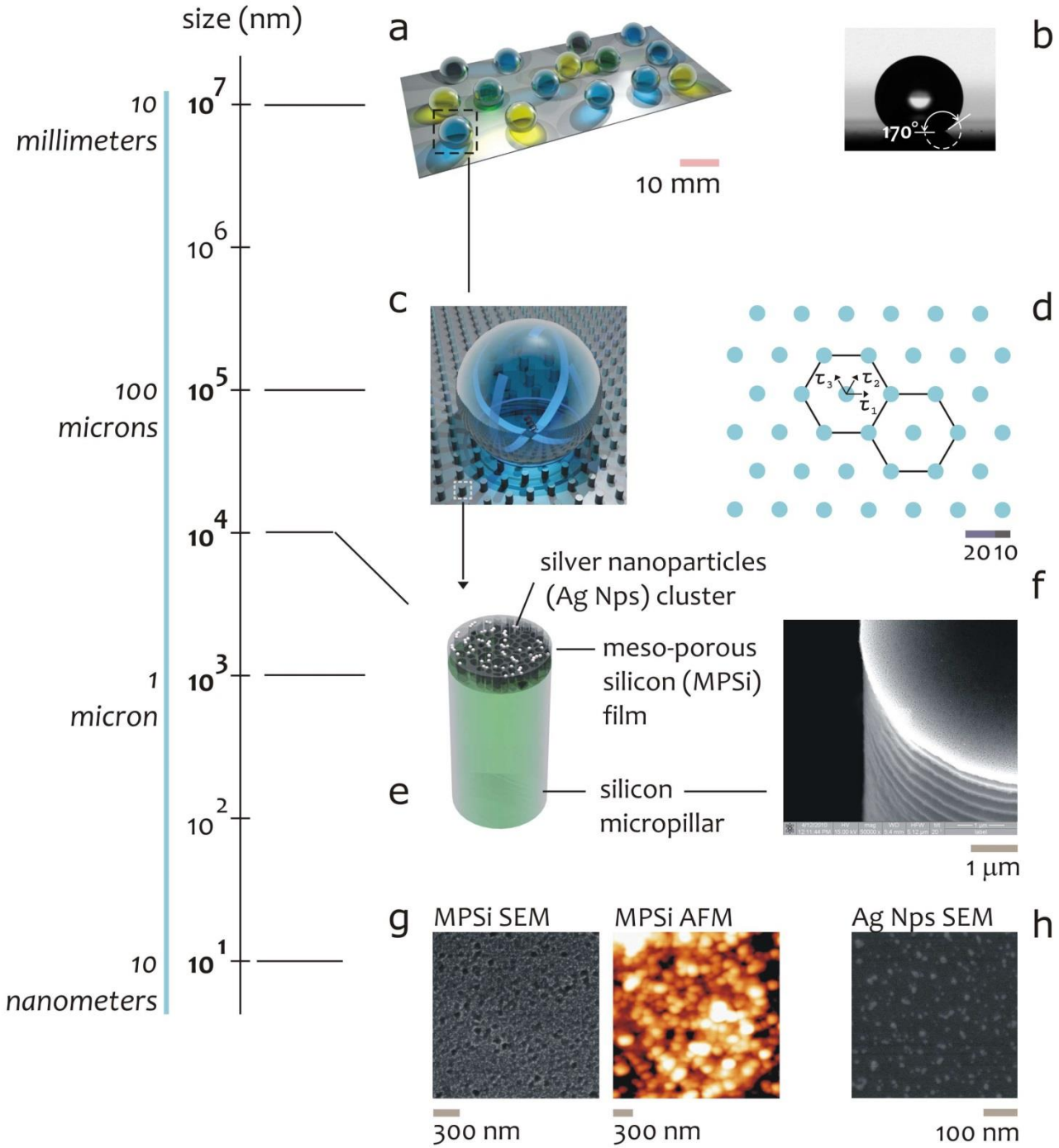

Fig. 1 at a continuum macro scale, the appearance of super-hydrophobic surfaces is that of a flat smooth plane (**a**) where drops maintain a nearly spherical shape (**b**). At a smaller micro scale, a periodic, regular array of cylindrical pillars is responsible for the non-wetting behaviour of the device (**c**, **d**). In the present work, the micro-pillars are modified to incorporate a meso-porous silicon film, in which networks of silver nano-particles are deposited (**e**, **f**).

SEM and AFM (**g**) micrographs reveal the morphology of the porous matrix at the nano-scale. Ultrahigh resolution SEM image shows the silver nanoparticle ensemble infiltrated into the pores (**h**).

The major advance of the device is its capability of combining different structures and functions that arise because of its hierarchal small scales. Those functions can be possibly used for the quantitative analysis of the low molecular weight fraction of blood, that has great relevance in medicine because the nature of this information can provide insight into the manifestation and development of a disease[41, 42]. In this work, this device was verified using an artificial, binary solution of Rhodamine and Albumin molecules, which have different molecular masses and thus sizes. Rhodamine is a *small* molecule, with a molecular weight of about 500 Da; differently from Rhodamine, Albumin is a *large* molecule, with a molecular weight approaching 6×10^4 Da, that is nearly 2 orders of magnitude higher than that of Rhodamine. Therefore, Rhodamine may be taken to represent the low molecular weight fraction (that discloses the large majority of the information content) of a solution of biological interest. In what follows, the device was utilized to separate from the solution and analyze Rhodamine in the considerably low abundance range of 10^{-16} molar.

This scheme may be of interest for the very large community of researchers working in the field of biomedical devices and molecular diagnostics, where the most severe limitation of current approaches is the difficulty of handling extremely low concentrated solutions containing few molecules.

The paper is organized as follows. In the experimental section: we describe the methods utilized to fabricate and characterize the device, and to conduct the spectroscopy measurement of the biological samples (§2). In the results: we present the final device (§3.1) and demonstrate the ability of the described device to capture and measure few small Rhodamine molecules from a biological solution (§3.2), these two paragraphs represent the *experimental* verification of the samples. Moreover: we show how the complex geometry of device, with its two scale roughness, delivers the ability to manipulate, transport and, ultimately, capture few molecules with an increased efficiency compared to simpler flat surfaces (§3.3); using theoretical models and computer simulations, we calculate the electromagnetic field enhancement in a self-similar fractal set of metallic nanoparticles (§3.5) in opposition to mono-dimensional linear chains of metallic nanoparticles (§3.4); these three paragraphs, constitute the *theoretical* framework which explains or supports the findings of the paper, and may help to challenge and extend the cited results. In the conclusions: we briefly review the results and propose possible directions for future work.

2 Experimental Section

Super-hydrophobic surfaces were realized. Those surfaces comprise micro pillars disposed on the substrate to form a regular hexagonal motif (**Fig.1c,d**); the pillars were then modified to incorporate meso-porous silicon films (**Fig.1e-g**). Silver nanoparticles were infiltrated into the pores to guarantee superior SERS capabilities (**Fig.1h**). FIT (Finite Integration Technique) calculations verified the ability of aggregates of silver nanoparticles to give maximum electromagnetic fields which are a factor of 10 larger than any compact monomer structure. On account of their hierarchical structures bridging different length scales, those devices exhibit an increased hydrophobicity with contact angles as large as 170° [12]. Small drops (V<10 μl) of a solution of Rhodamine and Albumin with a concentration as low as 10^{-16} M were gently positioned upon the surfaces and the entire process of evaporation followed over time; depending on the droplet size, the evaporation time takes from few minutes to nearly 30 minutes. An automatic contact angle meter (KSV CAM 101, KSV Instruments LTD, Helsinki, Finland) was used at room temperature. Please notice that the energy of adhesion γ per unit area at the gas/water interface is ~72.8 mJ/m^2 at 20 °C. The evaporation processes were performed in a clean room to reduce the presence of external contaminants and lasted approximately 30 min. Prior the full impalement of the drop, the sample was removed by using a pipettor. The residual solute was observed using scanning electron microscope (SEM), fluorescent microscopy and Raman spectroscopy techniques. Rhodamine (R6G) and bovin serum Albumin (BSA) were purchased from Sigma. Deionized water was used for all experiments. All chemicals, unless mentioned elsewhere, were of analytical grade and were used as received.

2.1 Micro-fabrication of patterned Super-hydrophobic surfaces. The patterned surfaces were characterized by periodic hexagonal tilings of cylindrical pillars. The diameter d and the distance l between the pillars were chosen in accordance with a criterion of optimal design described in previous works [7, 22], that is d=10 μm and l=20 μm; while the height of the pillars was h=10 μm. In doing so, a small fraction of solid $\phi=\pi/4\ d^2/(l+d)^2\sim0.09$ was secured, assuring an increased hydrophobicity with contact angles approaching 170°, with ϕ still sufficiently large to prevent the collapse of the drop at the early stage of evaporation. *P*-doped, (100) silicon wafers with resistivity of 5–10 Ohm/cm were used as substrates; they were cleaned with acetone and isopropanol to remove possible contaminants and then etched with a 4% hydrofluoric acid (HF) solution. The wafers were then rinsed with deionized water and dried with N_2. Standard optical lithography techniques (Karl Suss Mask Aligner MA 45, Suss MicroTec GA, Garching, Germany) were employed to obtain regular patterns of disks within a layer of negative tone resist (AZ5214) that was spin-coated onto clean silicon wafers. The masks necessary for optical lithography were fabricated using standard Electron Beam Lithography (Crestec CABL-9000C Electron beam lithography system) methods. The disks served as a mask in a Deep Reactive Ion Etching Process (DRIE) (MESC Multiplex ICP, STS, Imperial Park, Newport, UK), whereby the final structures were obtained in the form of cylindrical pillars with an aspect ratio greater than 2. The DRIE process utilized was a pulsed, time-multiplexed etching that alternates repeatedly between two modes, and namely (i) an isotropic plasma etch, where SF6 is used, and (ii) a deposition of a chemically inert passivation layer, that is C_4F_8, as described in the paper of Limongi and colleagues [30]. On removing the residual resist with piranha solution, the substrates were prepared for the formation of a meso-porous silicon film (H_2SO_4:H_2O_2=3:1 v/v).

2.2 Formation of the Meso-porous Silicon matrix. Porous substrates with a pore diameter lower or equal to 5 nm were obtained by anodization of the silicon micro pillars using an electrolyte mixture of HF, D.I. water, and ethanol (by Sigma-Aldrich) (1:1:2, v/v/v) as described, for instance, in Foll et al. [43]. The sample comprising the silicon micro-pillars was placed in a teflon electrolytic cell, where a platinum cathode and the silicon wafer (anode) are immersed in a hydrogen fluoride (HF) solution. A constant current density of 20 mA/cm^2 for 5 min at 25°C was applied. The photoluminescence properties of the PSi substrate were directly verified using an ultraviolet lamp (from Spectroline) in the long wave ultraviolet limit (365 nm). The lamp was positioned at 25 cm from the sample, a distance that guarantees a typical peak intensity density of 1000 μmW/cm^2. The UV illumination was maintained for 10 s, and the samples were photographed with a commercial camera (Canon) setting 2 s integration time. Surface hydrophilicity of the samples was determined by measuring the water contact angle with one drop of about 5 μl of D.I. water using an automatic contact angle meter (KSV CAM 101, KSV Instruments LTD, Helsinki, Finland) at room temperature. Four measurements were performed on each substrate to evaluate the average contact angle θ, at 5 s.

2.3 Electroless deposition of silver NPs. Silver nano-grains were implanted into the porous matrix to obtain devices with advanced sensing capabilities. To do so, the sample of meso-porous silicon micro pillars was immersed in a solution of silver nitrate ($AgNO_3$) and hydrofluoric acid (HF). An electroless process selectively assembled silver atoms into supra-molecular nano-particles into the pores. Electroless deposition is a process whereby ionic silver is reduced and deposited as metallic silver upon silicon via a redox reaction, as explained in the work of Coluccio and colleagues [39]. The electroless deposition on a substrate is based on an autocatalytic or a chemical reduction of aqueous metal ions, where an electron is exchanged between metal ions and a reducing agent. Here, the meso-porous silicon matrix was used itself as reducing agent. In depositing the silver nanoparticles, the concentration C of solution of the $AgNO_3$ silver salt, the time of deposition t, and the temperature T, were hold fixed, being C=0.1 mM, t=60 s, T=50° C. After growth, the sample was rinsed with water and dried under nitrogen flux.

2.4 SEM characterization. Several SEM images of the samples were captured to assure reproducibility and repeatability, utilizing a Dual Beam (SEM-FIB) - FEI Nova 600 NanoLab system. During the acquisitions beam energies of 5 and 15 keV, and corresponding electron currents of 0.98 pA and 0.14 nA, were used. The silver nano-grains were verified using the compositional analysis, whereby the low angle backscatter (LABe) detector allows unprecedented contrast that clearly differentiates between the silver particles and the porous silicon matrix. In some cases the mode 2 configuration was set, through which images can be magnified over 2500×10^3 times, and ultra-high resolution can be achieved.

2.5 AFM characterization. Atomic force microscopy (Veeco MultiMode with NanoScope V controller) was used for the measurements of the meso-porous structures. All the measurements were performed in a dry environment in intermittent contact mode over a sampling area of 500×500 nm^2. Room temperature was hold fixed for all the acquisitions. Ultra-sharp Si probes (ACLA-SS, AppNano) with a nominal tip radius less than 5 nm were used for achieve high resolution. Multiple measurements were done in different scan directions to avoid artefacts. At least four images in height mode (trace and retrace) were recorded per sample. The images had a resolution of 1024×1024 points and were acquired at a scanning rate of 1 Hz. The obtained images were processed with the WSxM® software, using either flattening or plane fit according to the relief characteristics, with the minimal polynomial order needed. The characteristic average surface roughness (R_a) was thus deconvoluted for each substrate. Using conventional mathematical procedures implemented in Mathematica®, a power spectrum (PS) and corresponding fractal dimension, were further derived for each image.

2.6 Raman characterization of Rhodamine deposits. The Rhodamine deposits were observed using Raman spectroscopy techniques. Micro-probed Raman spectra were obtained using Renishaw inVia Raman microscope at room temperature through 20x/50x objectives of a Leica microscope. The Raman spectra were excited by the 514.0 nm line of an Ar+ laser in backscattering geometry. The laser power was hold constant at 0.18 mW with an integration time of 20 s. The interferograms were recorded with a resolution of 2 cm^{-1} and were averaged over 5 samples. Each spectrum was base line corrected with a second degree polynomial function after acquisition. Mapping Raman measurements were performed with step size of 15 μm and 12.9 μm in x and y-axis direction, respectively.

2.7 Fluorescence microscopy verification of the samples. Fluorescence microscopy measurements were performed using an upright microscope with infinity-corrected optics (Zeiss LSM 780NLO). The microscope objective used was a Zeiss W Plan-Apochromat 40x with 1 numerical aperture. For probe excitation a diode-pumped solid-state (DPSS) laser source emitting at 561nm was used. After assembling the surfaces on the stage, a region on the sample was chosen for measurement (region of interest). The flow of the trace in the region of interest was recorded during the whole experiments. Each experiment lasted less than 450 s. The size of the region of interest was of 212×212 μm^2 and it was mapped into 1024×1024 points. An acquisition rate of about 1/10 fps was set for the experiments, that is sufficiently fast to follow the transport of the trace within a slowly evaporating droplet. Each acquired frame was then converted and exported to Mathematica®, where it was analyzed by means of standard image-analysis tools.

2.8 FIT simulations. The simulations of the EM field around the clusters of silver nano-grains were performed by using the FIT (Finite Integration Technique) numerical method. This approach is especially suitable for dimensionally large structures when compared to the wavelengths of interest. The method, introduced by Thomas Weiland in 1977, is based on the integral form solution of the Maxwell equations. Similarly to other numerical approaches, it is very sensible to the mesh definition, therefore convergence mesh analysis was performed in order to assure the stability of the results. This analysis led to a local spatial resolution down to 1nm. Here, all the simulations have the same mesh density, hence to allow a direct comparison among the

results obtained at different polarization angles. Furthermore, the same mesh density was maintained between the two sets of particles. In the present case, we have adopted tetrahedral mesh, which is especially suitable for curved surfaces. In this way, it can be estimated an error on the far field calculations below 1%.

3 Results and Discussion

3.1 Realizing the super-hydrophobic surfaces. Several SEM micrographs of the super-hydrophobic devices were taken over different samples to assess uniformity and reproducibility. In

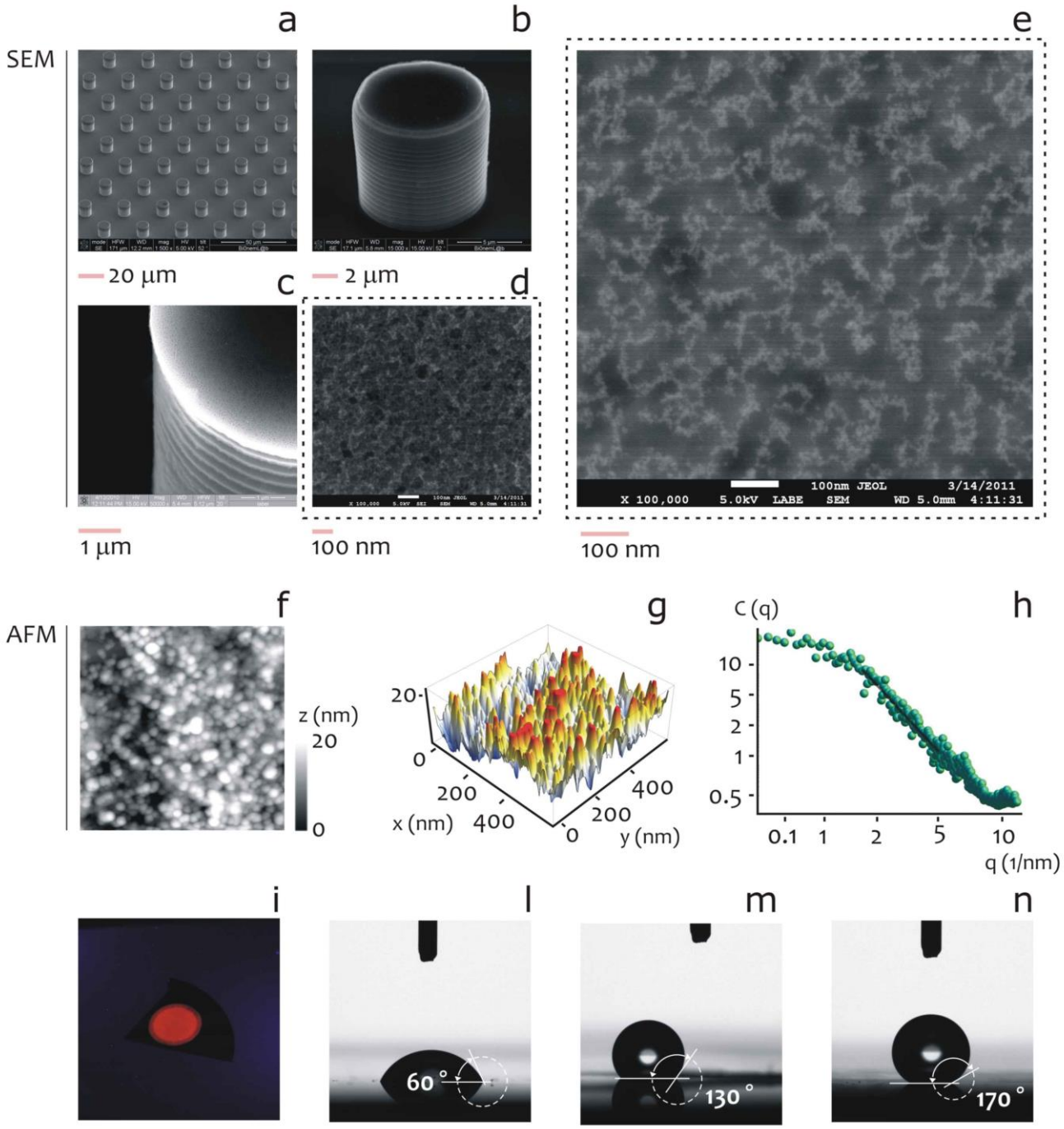

Fig. 2 Several SEM micrographs of the super-hydrophobic devices were taken over different samples to assess uniformity and reproducibility. Si pillars are arrayed over large square areas sizing up to some hundreds of micrometers per side. This would verify the fabrication process capability to attain extreme control over the key characteristics of the micro-pillars such as shape and size on a large scale (**a**). On a smaller scale one can notice the exposed top surface of the pillars covered by the meso-porous silicon film (**b, c**). An ultra-high resolution image, with a 10^5× magnification factor, reveals the morphology of the meso-porous matrix (**d**). The silver nanograins distribution is verified using a SEM compositional analysis, where the low angle backscatter detector distinctly differentiates between the silver particles and the porous silicon matrix (**e**). The topology of the meso-porous silicon matrix

was further verified through AFM imaging (**f, g**). A power spectrum was conveniently derived (h) and used to estimate the effective fractal dimensionality D_f of the meso-porous film, D_f~2.8. The pore size distribution in the low nanometer range is confirmed by the photoluminescence analysis where the device is exposed to a UV light (**i**). The contact angle of pure silicon approaches 60° (**l**), while the flat meso-porous silicon matrix exhibits a contact angle of nearly 130° (**m**). In opposition to this, the fabricated micro-nano structure features contact angles as large as 170° (**n**).

Fig.2a, silicon pillars are arrayed over large square areas with size as large as some hundreds of micrometers, with no or minor defects in the structures which thus recover a perfect hexagonal lattice. This would verify the fabrication process capability to attain extreme control over the key characteristics of the micro-pillars such as shape and size on a large scale. On a smaller scale, as in **Fig.2b,c**, one can notice the exposed top surface of the pillars covered by the meso-porous silicon film. This is even more evident in **Fig.2d**, where an ultra-high resolution image, with a 10^5× magnification factor, reveals the morphology of the meso-porous matrix, where the pore size is in the low nanometer range.

For estimating the pore size distribution in the porous substrates, we used ultra-high resolution SEM images. These images have a sufficient level of detail to allow a precise evaluation of the pore size distribution in the low meso-porous regime, that is, for pores larger than 2 nm, even without the need of adsorption/desorption isotherms. From these images, using image analysis algorithms used and described in[44], we derived the average pore size as S=5 nm. Notice that the pore size distribution may have tails that reach and surpass the 10 nm, and in fact the presented devices still harvest a reduced, and not null, amount of large Albumin molecules, as correctly indicated in the Results section. Additional SEM images of the pore substrates were conveniently included in a separate **Supporting Information file #1** to further verify the pore size distribution.

Differently from the meso-pores in the meso-porous matrix, the silver nano-grains distribution was verified using a SEM compositional analysis, where the low angle backscatter detector allows high contrast that distinctly differentiates between the silver particles and the porous silicon matrix. **Fig.2e** represents the ultrahigh resolution image of the same sample reproduced in **Fig.2d**, except that it was obtained using the described compositional analysis; here, the metal grains, in light gray clearly visible against a black background, are disposed in the plane as to reproduce random chains of nanoparticles, where the number of particles in a network varies over a significant range. Similarly to this, the particle size a varies around the average value a=10 nm, with a standard deviation s=1 nm. In a separate results section below, it will be discussed the capability of those chains to induce giant electromagnetic fields.

The SEM images presented in **Fig.2 d** and **e** reveal that the silver nanoparticles accumulate, for the large majority, along the edges of the nano-pores, without occluding the pores which still retain the ability to harvest and accommodate small molecules. This effect can be ascribed to a non-uniform distribution of surface energy density that is larger on the pore borders (or edges) compared to that on bulk, flat silicon[45-48]. The described increased energy density is responsible for the transport, sedimentation and growth the particles on the edges of the pores (for a thorough description of this mechanism, see the Appendix B in [49]). In a separate **Supporting Information file #2**, we include additional SEM images with further evidence of the described particles distribution.

These additional SEM images, along with the cross-sectional SEM images in **Fig. S2.8** (where the conditions of growth and the growth itself have been exaggerated for illustrative purposes) indicate that, while some AgNPs are occasionally deposited in depth in the pore matrix, the majority of those nanoparticles are localized close to the Z=0 surface, that is here defined as the interface between the original porous silicon sample and the upper air volume. Also, on observing the SEM micrographs, we recognize how these particles present a variable particle size, and this variation may be attributed, to a certain extent, to the pore size of the porous substrate.

The topology of the meso-porous silicon matrix was further verified through **AFM** imaging, as in **Fig.2 f,g**. From this, using custom made algorithms, a power spectrum was derived (**Fig.2h**) and used to estimate the effective fractal dimensionality D_f of the meso-porous film. This dimensions, for the particular set of experimental parameters used here, has a value of about D_f~2.8, well in agreement with previous studies[44]. The fractal dimension is a parameter that can be used to describe intimately the topography of a variety of systems, especially at the nano scales[12, 50, 51]. It is an index for characterizing fractal patterns by quantifying their complexity as a ratio of the change in detail to the change in scale, therefore, it gives a measure of the complexity of those objects[50]. In this case, the nano-porous silicon matrix, conveniently formed on the top of the pillars, would give to the system a multi-scale, hierarchical structure. This structure, on bridging the micro and nano scales[12-14], is responsible for the artificial, increased hydrophobicity of the devices, with contact angles as large as 170° (**Fig.2n**). In comparison, the pristine silicon surface has a contact angle of 60° (**Fig.2l**), while the flat meso-porous silicon matrix exhibits a contact angle of nearly 130° (**Fig.2m**). The pore size distribution is confirmed by the photoluminescence analysis where the device is exposed to a UV light (**Fig.2i**), the strong luminescence confirms the occurrence of pores in the low nanometer range[52].

3.2 Size-exclusion-based, elective capture and SERS measurements of small molecules. Here, we demonstrate that the presented devices are capable to concentrate, separate from a mixture, and measure small molecules in abundance ranges below the pico molar.

To do this, we prepared a solution containing a 1:1 binary mixture of Rhodamine and BSA (moles/moles, with initial concentration 10^{-16} M). We extracted a 10 µl droplet from this solution and spotted the sample on the device, where geometry (that is, the pillars) and the morphology (that is, the meso-porous film) combine to yield extremely large contact angles and thus very low friction coefficients (non-wetting behavior of the device). The evaporation process was then followed over time. The contact area of the drop at the liquid-solid interface was progressively reduced; the molecules, initially dispersed within the entire volume of the droplet, were transported into a small region of the substrate. Prior the collapse of the drop (that is,

before the irreversible transition to the Wenzel state), the sample was removed using a pipettor. The complex network of pockets and openings constituting the meso-porous film trapped those molecules with a hydrodynamic diameter $2r_h$ strictly smaller than the pore size; while larger molecules could be removed by the surface after multiple washings with deionized water. Considering that, for the present configuration, the average pore size is about 5 nm, R6G molecules, with a characteristic length size of r_h~0.5 nm, were secured to the substrate, while BSA proteins, with r_h~6 nm, were eluted. Micro-Raman mapping measurements were performed to confirm this assertion.

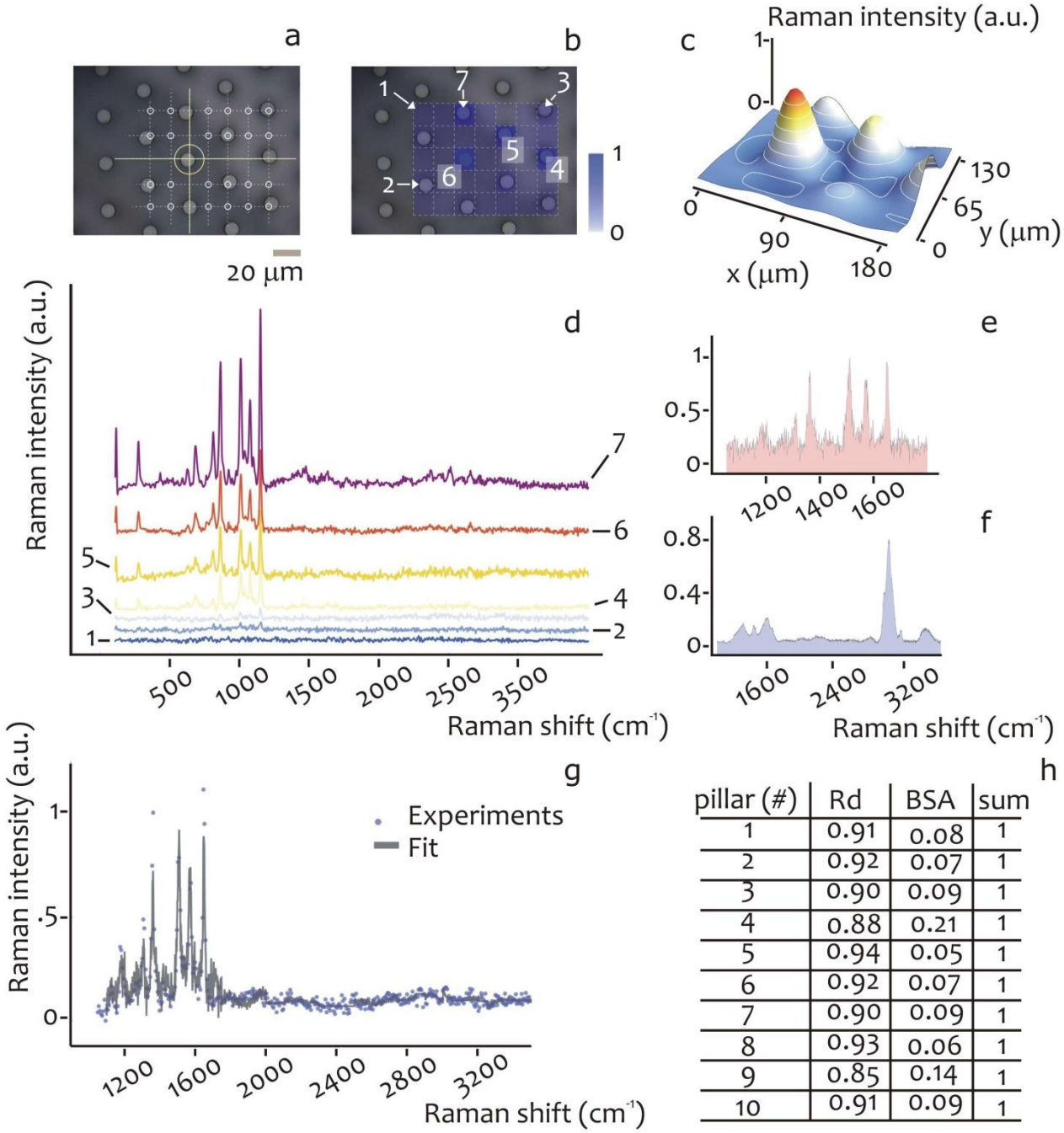

Fig. 3 top view of a range of meso-porous micro-pillars upon evaporation of a binary solution of Rhodamine and BSA. A Raman matrix scan was performed over the sample to verify the sensing capabilities of the device. The grid was positioned in the central region of the device, spanning over a sufficiently large number of pillars (**a, b**). The intensity profile of the sample is reported in the form of a raster (**b**) and a 3d plot (**c**). Single SERS spectra acquired in specific positions of the substrate are shown separately in (**d**). The characteristic fingerprint of Rhodamine (**e**) and BSA (**f**). A specific metrics is applied to estimate the relative abundance of Rhodamine and BSA molecules in the sample on a quantitative basis. Using a linear combination of the

Rhodamine and BSA spectra, the experimental spectra are fitted everywhere on the device, an example of which is reported in (**g**). From those fits, the relative content of Rhodamine and BSA are determined for all the pillars in the considered range of acquisitions (**h**).

A matrix scan was performed over a rectangular grid as explained in the Supporting Information (**Fig.3a**). The grid was positioned in the central region of the device, spanning over a sufficiently large number of pillars. In **Fig.3b,c**, the intensity profile of the sample is reported in the form of a raster and a 3d plot, respectively, where the interpolated 3d map in **Fig.3c**, derived using a polynomial curve fitting of order three, exhibits a sub-pixel resolution. Those profiles were derived using as a reference a band centered at 1660 cm^{-1} (**Fig.3e**), that typically characterizes Rhodamine deposits. Therefore, the plots reported in **Fig.2 3,c** show the Rhodamine content over the considered domain, and notice that the distribution of Rhodamine in the plane is consistent with the packing of the pillars in an hexagonal lattice. Also notice, from **Fig.3c**, three peaks, in a triangular pattern, corresponding to the points where the capture of Rhodamine molecules was especially efficient.

The single SERS spectra acquired in specific positions of the substrate are shown separately in **Fig.3d**. All the spectra are pretty similar in shape, that is, the principal peaks are preserved moving from a point to another, and this would guarantee that SERS measurements are repeatable. More important than this, it is evident how those spectra are very similar to the characteristic fingerprint of Rhodamine (**Fig.3e**), in comparison to the reference spectrum of BSA, to which instead the experimental spectra differ to a great extent.

A specific metrics was then applied to estimate the relative abundance of Rhodamine and BSA molecules in the sample on a quantitative basis. Using a linear combination of the Rhodamine and BSA spectra reported in **Fig.3e,f** as a basis, the experimental spectra were fitted everywhere on the device, as explained in the **Supporting Information file #3**, an example of which is reported in **Fig.3g**. From those fits, the relative content of Rhodamine and BSA were determined for all the pillars in the considered range of acquisitions. The results, reported in the table of **Fig.3h**, show that the content of Rhodamine exceeds the 90% for all the pillars in the considered range of acquisitions, and this would demonstrate the initial assertion that, on a similar device, the separation and detection of the low molecular weight content of a diluted mixture is effective.

In addition to this, we realized supplementary (independent) experiments to verify even further the harvesting abilities of the presented meso-porous devices, as reported in the **Supporting Information file #4**. We prepared solutions of (i) Rhodamine in D.I. water, (ii) Albumin in D.I. water, and (iii) a mixture of Rhodamine and Albumin in D.I. water in different concentrations ranging from 10^{-6} (that are, concentrated solutions) to 10^{-12} M (that are, diluted solutions). Upon incubation of the porous devices with the described solutions, we verified the release of molecules over time using UV-VIS spectroscopy techniques. The results (**Fig. S4.1**) demonstrate that the samples previously loaded with Rhodamine (i) show an effective release over time; differently from Rhodamine (ii), the samples incubated with the solutions containing Albumin do not show an appreciable release at any time. Finally, in line with the described results, the samples incubated with the Rhodamine and Albumin mixture (iii) reveal a release curve that resembles, to a large extent, that of Rhodamine alone. The described results would confirm the ability of the devices to separate and select the low molecular weight content of a mixture, where the cut off size can be conveniently controlled on changing the pore size of the meso-porous film.

The Raman mapping measurements described above were carried on in correspondence of an ideal Z=0 plane which corresponds to the interface between the porous silicon matrix and the biological solution positioned above it. The average pore size is strictly larger than the hydrodynamic radius of Rhodamine and strictly smaller than the hydrodynamic radius of Albumin, that is why Rhodamine molecules are likely to be harvested by the device, and this has been thoroughly described in the text. If the captured molecules (or a fraction thereof) happen to be in close proximity to the clusters of silver nanoparticles, SERS effects are generated, and the signature of the cited Rhodamine molecules is available for reading and analysis even in very low abundance ranges. As explained above in the 3.1 Results section, the majority of AgNPs are localized at the plane Z=0. Nevertheless, a few silver nanoparticles may be randomly distributed within the pore matrix. It would be therefore sufficient that the captured Rhodamine molecules are intersected by the Z=0 plane to have an appreciable Raman signal. That is to say, target molecules may be recognized if are adsorbed to the most superficial layers of the porous surface.

After washing, larger Albumin molecules would be eluted and smaller Rhodamine molecules would be instead retained. The resultant gradient of concentration would induce an outward diffusion of Rhodamine: as a result, those molecules incorporated in the most internal compartments of the meso-porous silicon matrix would be transported towards the external Z=0 plane, thus increasing significantly the number of molecules that are candidate for SERS recognition (and, consequently, the Raman signal). After sample drying, those Rhodamine molecules would be irreversibly bound to the silicon matrix and be in an not-hydrated status. In this condition, no further fluxes would be possible, and the Raman measurement would be stable over time. The hypothesis of an outward flux of Rhodamine is indirectly confirmed by the release curves of Rhodamine over time in an aqueous environment, as reported in the **Supporting Information file #4**.

In separating Albumin from Rhodamine, a major issue is represented by the known ability of albumin to harvest and carry small hydrophobic molecules such as Rhodamine. Bovine (BSA) and Human Serum Albumin (HSA) may bind a broad range of hydrophobic small molecule ligands including fatty acids, bilirubin, thyroxine, bile acids and steroids; they serve as a solubilizer and transporter for these compounds and, in some cases, provide important buffering of the free concentration[53, 54]. Moreover, they bind a variety of drugs in multiple binding sites with high association constants ranging from ~10^4 to about ~10^5 (M^{-1})[55]. In particular, BSA may selectively bind Rhodamine B. In the work of Cai and colleagues [56] it was demonstrated that the specific binding constant of this interaction is 4.8 10^4 M^{-1} and the binding number of RB with BSA is 1.2:1.

In combining Albumin and Rhodamine in a solution, one would expect Rhodamine molecules to bind to Albumin, with the formation of one individual supra-molecular compound with loss of specificity and this would prevent the utilization of those meso-porous devices to separate selectively the low to the high molecular weight content of a solution.

Nevertheless, our devices were effective in capturing and selecting small molecules in solution, as demonstrated by the heretofore presented results, including Raman and UV spectroscopy measurements. Therefore, other mechanisms are responsible for this ability in opposition to the propensity of Albumin and Rhodamine to combine to form super-clusters. While a thorough understanding of a similar phenomenon would deserve a dedicated analysis and tractation thereof, here we *speculate* that these mechanisms or factors, are:

#1 the *reversible* binding of Rhodamine to BSA. The described protein-ligand (Albumin-Rhodamine) complex relies on a weak non-covalent hydrophobic interaction: even upon the formation of a BSA-Rhodamine complex, this unstable complex may degrade to disentangle back the single BSA and Rhodamine molecules, which would be available for separation using our nano-filter. Notice that this weak interaction is at the basis of strategies for the preparation of protein-based nano-delivery vehicles for hydrophobic active pharmaceutical ingredients[57-59].

#2 BSA-Rhodamine recognition is a diffusion limited process. The thermodynamics of recognition and interaction between BSA and Rhodamine cannot be lumped in the sole overall rate of association variable[60]. This indeed is a complex phenomenon, to understand which, and the mechanisms thereof, including the orientational motion of the ligand, its intrinsic nuclear motions, and the lifetime changes in the hydrophobic phase, one should employ sophisticated techniques such as femtosecond-resolved fluorescence[60]. In the work of Zhong et al. [60] and references therein, it is assumed that this association is diffusion controlled thereby the true molecular time scale of recognition is masked by diffusion. Nevertheless diffusion takes impractical time scales. Driven by pure diffusion, diluted molecules in a millimetric droplet would take minutes to hours to come in close proximity, interact, and finally bind to each other[61]. In contrast to this, the time scale of evaporation of the solution upon the super-hydrophobic surface is much lower[22]. In other words, evaporation dominates over diffusion. As a result, molecules in a solution would be transported towards the target meso-porous surface, and would be separated, before having the time to form individual complexes.

The described device integrates different hierarchical scales into one single chip. Some of these scales may expand the functionalities of conventional spectroscopy / spectrometry substrates including, as for some examples, DIOS (desorption ionization on silicon) devices, for application in mass spectrometry (MS). Where (DIOS-MS) is a matrix-less laser vaporization method for generating gas-phase ions[62], in which the physical properties of the silicon surfaces are crucial to DIOS performance[63].

The presented meso-porous super-hydrophobic devices should be ultimately used for separating the low molecular weight content from a real biological sample for analysis. Proteomics studies proteins systematically, especially pertaining their structure and function. In the long period, the goal of the project is providing proteomics with novel high tech procedures for the reliable early detection of cancers starting from serum, other biological fluids, or any sample obtained through minimally invasive or non-invasive techniques. The use of similar devices in conjunction with biological methods and advanced spectroscopy or spectrometry techniques, including SERS and MALDI-TOF, would yield bio-devices that integrate several analytical functions on a single chip, towards the early detection of tumors.

Nevertheless, to do this, biological sample preparation and pre-treatment are required or recommended. These may include SISCAPA (stable isotope standards and capture by anti-peptide antibodies) methods for specific antibody-based capture of individual tryptic peptides from a digest of whole human plasma. This or similar procedures should be developed and used prior any sample deposition and consequent Raman or MALDI-TOF analysis. Selected tryptic peptides of binding protein will be thus enriched relatively to a high abundance serum albumin peptide by some 20000-fold. The protein biomarkers are found in plasma in the ng/ml or pg/ml range, about 10 orders of magnitude below the major plasma proteins such as albumin. Using SISCAPA enrichment methods in conjunction to our super-hydrophobic devices, sensitivity of spectroscopy/spectrometry assay may be significantly increased to detect candidate protein biomarkers present in plasma around the ng/ml concentrations or below, with an outstanding advancement in the field.

While this paper is a proof of principle whose purpose is verifying that the presented devices are effective in separating and detecting low from high molecular weight molecules (where though Albumin has some biological relevance) in very low abundance ranges in water, the effective usage and applicability of this technology to biological fluids requires supplementary biological development and is left for future work.

If developed even further, this scheme may provide assistance and improve the efficiency of a large variety of processes that include, but are not restricted to, small-molecule analysis, quantitative studies, reaction monitoring, chromatography, protein identification and protein functional characterization, the analysis of reactions directed toward development of new catalysts and transformations.

3.3 Patterns of solute deposits on the device. The transport of a trace inside a slowly evaporating drop on a substrate and the consequent particle deposition is a complex phenomenon that has generated interest for the potentials in applications such as molecular sieves[64], optoelectronic devices[65], drug delivery[66, 67], and for the absorption and separation of the low molecular weight content of human plasma[68-70]. Despite its complexity, to a first approximation this mechanism can be regarded (and analyzed) as the superposition of simpler effects. These effects are: the displacement of particles inside an evaporating drop driven by convection and diffusion[71, 72], the translocation or capture of a molecule through a nanopore[69, 73-75].

Moreover, these effects depend upon the morphology of the substrate, in the sense that different substrate preparations would

affect the displacement and capture of target molecules. Specifically, the pattern of deposition produced during evaporation depends upon the flow within the drop that, in turn, is a function of the evaporative flux, the shape of the free surface and its porosity, the behavior of the contact line[71, 72].

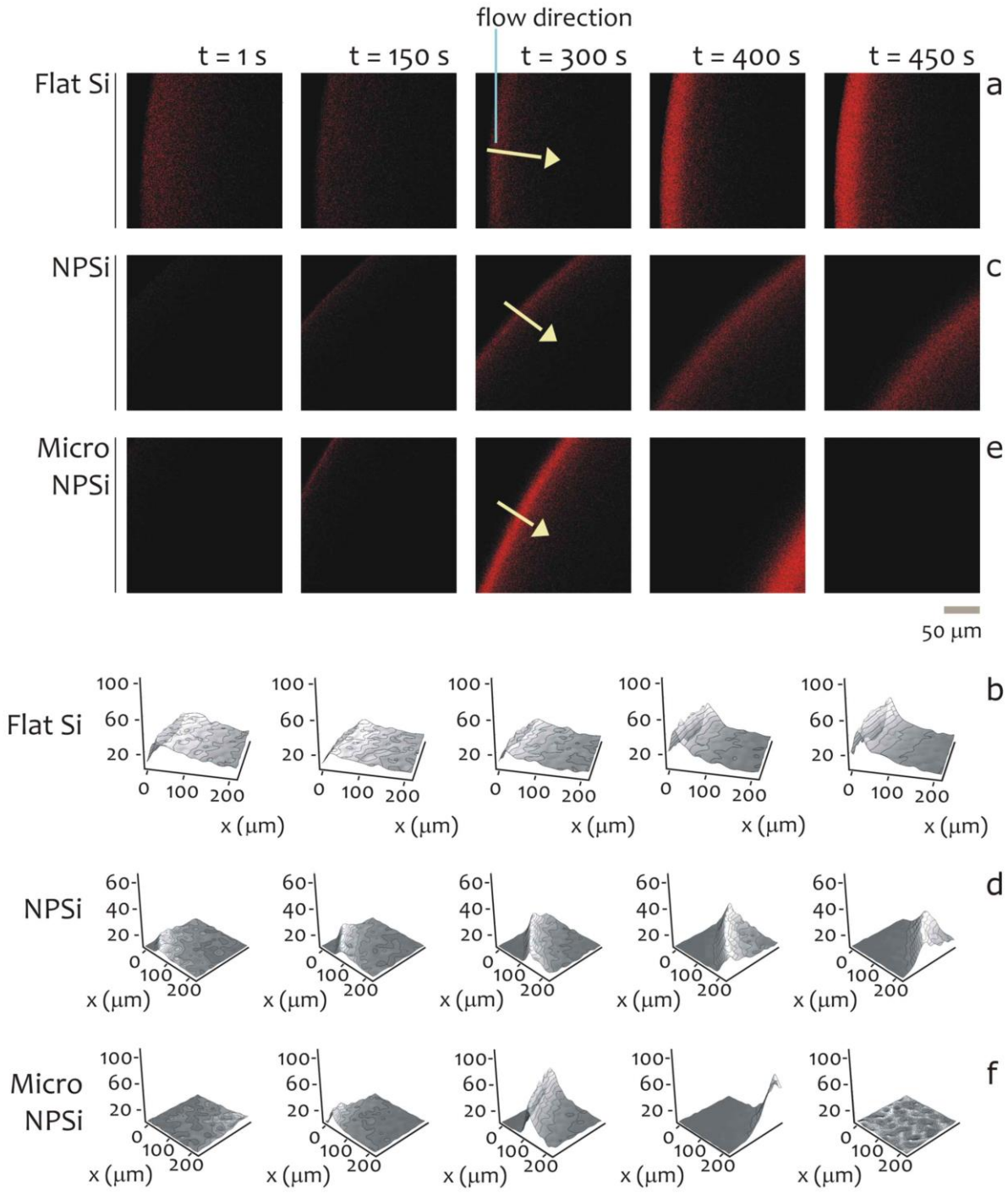

Fig. 4 confocal images reveal the distribution of Rhodamine molecules in a slowly evaporating droplet as a function of time on different substrates. On a flat silicon surface the drop of is pinned, and as it dries on the surface, it leaves a dense, ring-like deposit along the perimeter (**a**). This is even more evident in (**b**) where it is reported a quantitative 3D representation of solute distribution over time. The dynamics of evaporation and solute transport is followed for a meso-porous surface in (**c**, **d**). For this configuration, the hypothesis typically responsible for the ring formation breaks down, and the front of the deposit moves with time. This effect is even more

pronounced in (**e**, **f**), where Rhodamine is deposited on a micro patterned/meso porous super-hydrophobic surface. The velocity of the receding contact line is larger than for the other configurations, and at the final time of evaporation the solute has been completely depleted from the region where the drop was originally deposited.

The behavior of a particle in a flow can be described by Langevin equation[73, 76]

$$m\frac{\partial u}{\partial t} = 6\pi\mu a\left(K_p\boldsymbol{u} - K_f\boldsymbol{v}\right) + \mathbf{F_E} + \mathbf{F_B} \quad (1)$$

where **u** is the velocity vector for the particle, **v** is the unperturbed fluid velocity, *a* is the particle radius, and *m* is the particle mass. The first term on the right-hand side of Eq.(1) represents the hydrodynamic drag on the particle, while the second and third terms account for the electrostatic ($\mathbf{F_E}$) and Brownian ($\mathbf{F_B}$) forces. K_p and K_f are diagonal matrices describing the additional hydrodynamic hindrance associated with interactions between the particle and the system boundaries. Numerical, analytical and semi-analytical solutions of Eq.(1) have been provided for a variety of configurations all involving, to different extents, certain simplifying assumptions that make the theory to deviate from real systems, sometimes significantly. Here, differently from other theoretical methods, an experimental approach is adopted. Confocal images in **Figure 4** reveal the distribution of Rhodamine molecules in a slowly evaporating droplet (see Methods) as a function of time on different substrates.

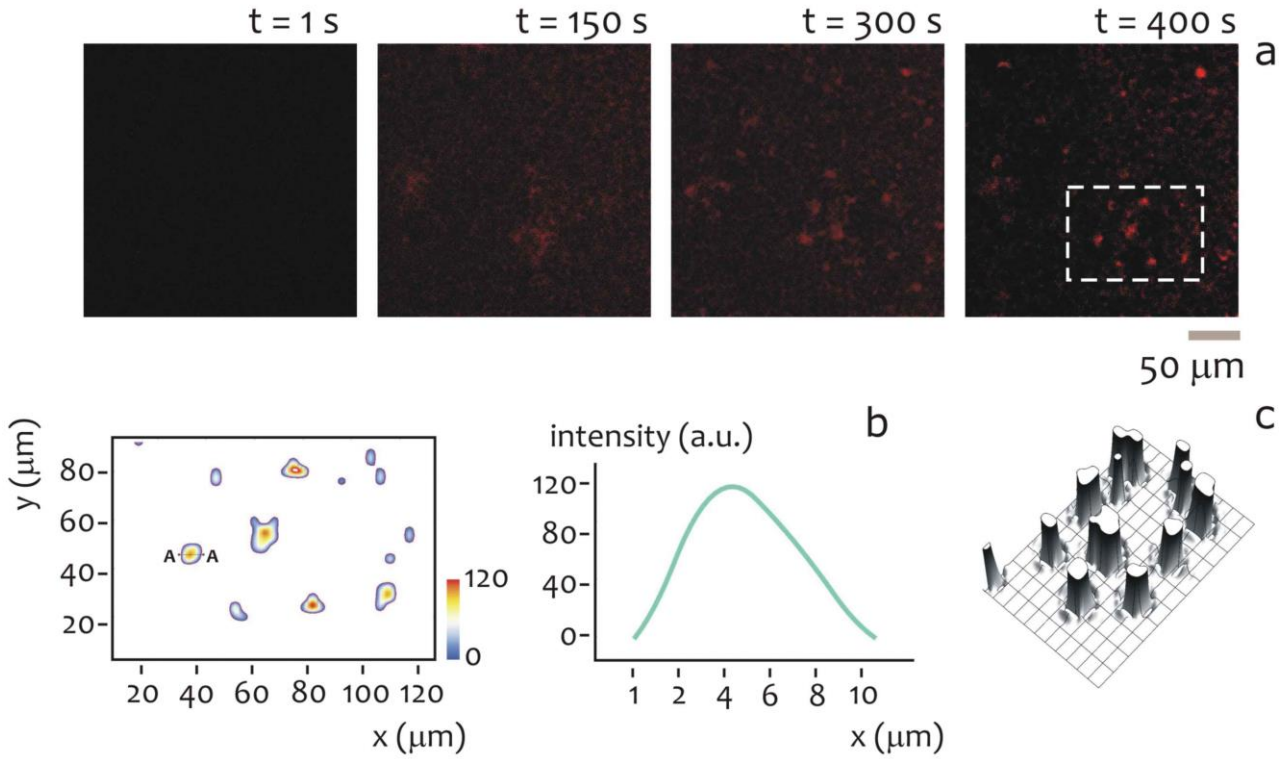

Fig. 5 the central region of the drop is imaged over time (**a**). The occurrence of a pattern of deposition is revealed already after 150 s from the injection of the solute on the substrate, using a temperature color scheme (**b**) and a 3D relief plot (**c**). For a meso-porous micro-structured surface, the transport and uptake of small molecules from few meso-porous pillars is effective.

On a flat silicon surface, as in **Fig. 4a**, the drop of is pinned, and as it dries on the surface, it leaves a dense, ring-like deposit along the perimeter, well in agreement with the literature[77]. This is ascribed to a form of capillary flow in which pinning of the contact line of the drying drop ensures that liquid evaporating from the edge is replenished by liquid from the interior. The resulting outward flow can carry virtually all the dispersed material to the edge. This is even more evident in **Fig.4b**, where it is reported a quantitative 3D representation of solute distribution over time. In **Fig.4 c,d**, the dynamics of evaporation and solute transport is followed for a meso-porous surface. Here, the contact angle is greater than for the flat, smooth silicon surface (**Fig.2**), with a consequent reduction in the friction coefficient of the substrate. In this case, the hypothesis typically responsible for the ring formation breaks down, and in fact the front of the deposit moves with time (**Fig.4d**). Notice that the

particles are not captured by the pores, and are instead pushed away by the moving contact line of the evaporating drop, possibly because the velocity of the receding line is greater than that necessary for particle uptake. This effect is even more pronounced in **Fig.4 e,f**, where Rhodamine is deposited on a micro patterned/meso-porous super-hydrophobic surface. The velocity of the receding contact line is larger than for the other configurations, and at the final time of evaporation (that is, 450 s), the solute has been completely depleted from the region where the drop was originally deposited. Notice that, in this case, the field of view of the microscope is adapted to the outer diameter of the drop, while the inner region is instead disregarded.

On imaging the central region of the drop over time (**Fig.5a**), the occurrence of a pattern of deposition is revealed already after 150 s from the injection of the solute on the substrate. Different visualizations of the same pattern using a temperature color scheme (**Fig.5b**), and a 3D relief plot (**Fig.5c**), clearly indicate that, for a meso-porous micro-structured surface, the uptake of small molecules from few meso-porous pillars is effective. Taken together, these results demonstrate that a substrate with a two scale roughness, from micro to nano, can manipulate, transport and, ultimately, capture few molecules in a solution in specific sites of the substrate in a predictive fashion.

3.4 Increased optical response of mono-dimensional linear chains of metallic nanoparticles. Electroless growth is an innovative technique in which metal ions are reduced and deposited as metals upon a silicon surface[78-80] or, more in general, on a reducing surface[39].

X

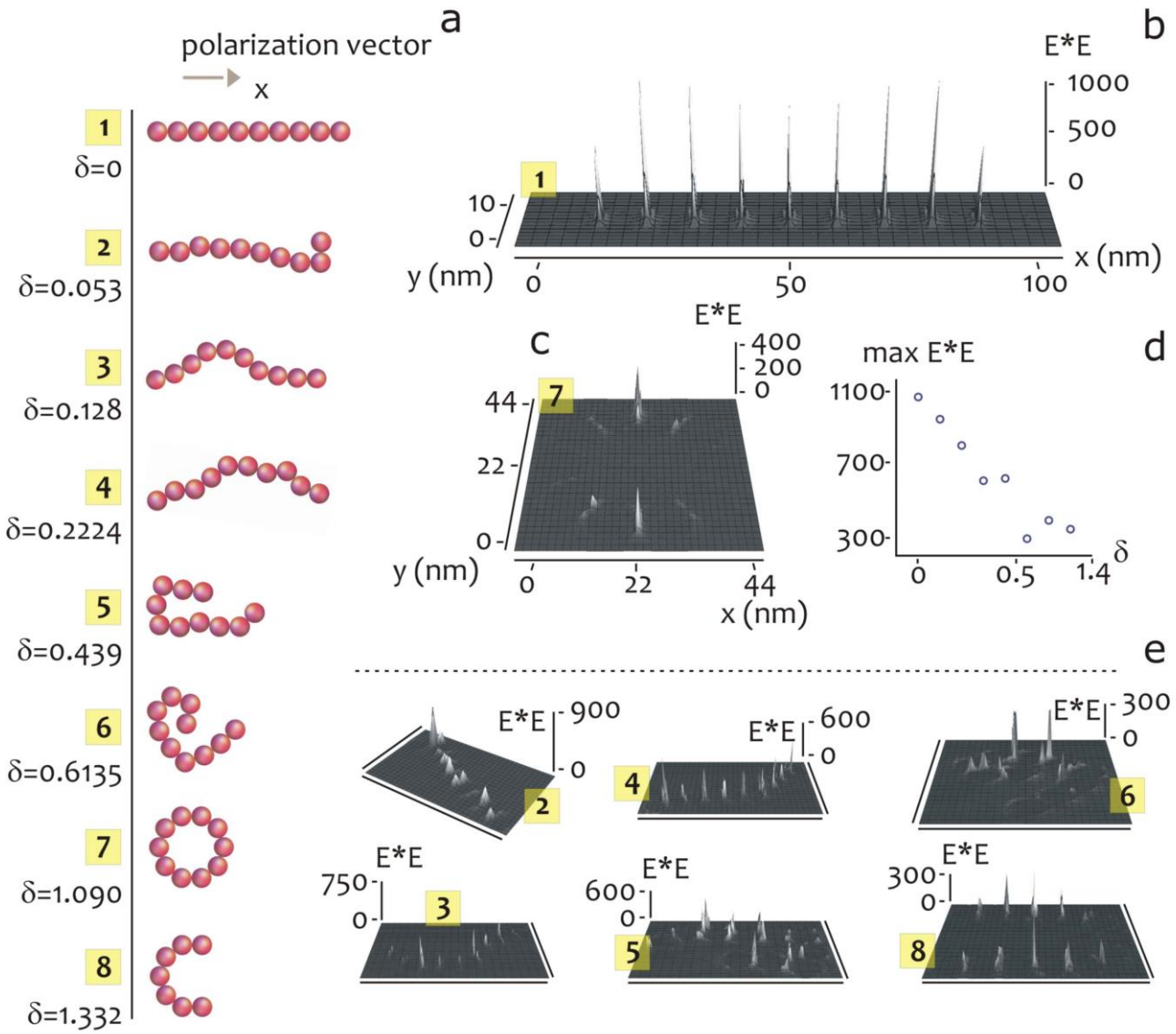

Fig. 5 numerical nanoparticles chains are shown in order of increasing disorder (**a**). The simulated EM field enhancement for a linear (**b**) and circular (**c**) chain of nanoparticles. The maximum EM field intensity as a function of the disorder parameter δ (**d**). Contour plots of the EM field for different nanoparticles configurations in the plane (**e**).

Here, electroless deposition was utilized for obtaining, on the top of the meso-porous pillars, disordered aggregates of silver nano-

particles. Similar geometries reveal a complex structure (with details over multiple scales) that may locally enhance the electromagnetic field, in contrast to isolated spheres, in which $|\mathbf{E}|^2$ peak values are relatively modest (~100). Self-assembled clusters of metallic nanoparticles separated by nanometric gaps generate strong plasmonic modes that support both intense and localized near fields[81, 82]. The topology of those silver grains is responsible for an increase of the electromagnetic radiation at the interface with the metal, and this is the well-known SERS effect[83]. SERS is a phenomenon whereby the electromagnetic field, at the close proximity of metal nano-clusters, is locally enhanced on account of the resonant interaction with the surface plasmons in the metal[83]. For all this, understanding how the distribution of silver nanoparticles in a network influences the local electric field, can improve the detection sensitivity limit of conventional Raman Spectroscopy and would boost the use of similar devices for sensor applications.

The SEM image in **Fig.2e** reveal the shape, size and distribution of the metal nanoparticles aligned along the edge of the nano-pores. Those are disposed in complex random patterns, where the size of the particles a~10 nm varies over a small range. In what follows, we describe the optics of similar clusters starting from a systematic study of isolated one-dimensional chains with incremental disorder. In doing so, we argue that considering the optical resonances of the constituent one-dimensional chains of the clusters is indeed useful to reach conclusions about the local and global behavior of the whole structure. In addition to this, in another paragraph, we describe the response of a bi-dimensional, somewhat more complex fractal set of metal nanoparticles.

In analyzing the optical response of random patterns of silver NPs, we consider ensembles of N=10 silver NPs with a diameter of a=10 nm. In **Fig.6a**, these nano-chains are presented in order of increasing disorder. The disorder parameter δ is here defined as the circular standard deviation of the angles α between the axis of each dimer of particles and a direction r assumed as a reference. Notice that δ does not depend on the choice of r.

$$\delta = \left(-2ln \left| \frac{1}{N-1} \sum_{i=1}^{N-1} e^{j\alpha_i} \right| \right)^{1/2} \quad (2)$$

The structures in **Fig.6a** range from perfectly straight (δ=0), to circular (δ=1.090), to highly disordered (δ=1.332). All the particles are contained in the xy plane where the x axis is the polarization direction. In FIT calculations for silver nanoparticles chains in which the degree of disorder of the nanoparticles were varied over a significant range, we found that these structures give maximum **E**-fields that are a factor of 10 larger than any compact monomer structure. Moreover, we observed a high sensitivity to δ.

In **Fig.6b**, a 3d plot of the electromagnetic field intensity is reproduced as a function of the spatial variables x and y for a linear string of particles. For this configuration, δ=0 and λ=630 nm. We observe that the maximum EM enhancement is reached at the particle-particle interface for the range of considered particle dimers. Accordingly, N-1=9 amplification points are observed on the substrate, and here the intensity of the EM field $|\mathbf{E}|^2$ ranges from 500 to over 10^3. In **Fig.6c**, the EM field intensity is reported for a circular annulus of nanoparticles, where δ=1.090. Differently from the linear configuration, here the optical resonance points of the system are found where the connection line of couples of adjacent metallic particles is parallel to the direction of polarization, and this is verified in two hot spots solely. Also notice that the maximum EM field, $|\mathbf{E}|^2$~300, is reduced compared to the linear configuration. In **Fig.6e**, the 3D plot of $|\mathbf{E}|^2$ is reported for all the remaining configurations. In general, the maximum intensity of the EM field depends on δ, and thus on the geometrical conformation of the system, as shown in **Fig.6d**, where $|\mathbf{E}|^2$ is reported for δ ranging from 0.053 to 1.332. Collectively, these findings demonstrate that the optical response of clusters formed by strongly interacting plasmonic nano-spheres depends on the degree of disorder of those clusters. For an ideal linear system (δ=0), the intensity attains a maximum, while it decreases for increasing δ. For disordered systems (δ>0.5), $|\mathbf{E}|^2$ drops below 300, that still is a factor of 3 larger than the electromagnetic field generated by any isolated dimer. Considering that the intensity of the Raman signal is proportional to the fourth power of the electric field, the Raman signal from molecules adsorbed on these surfaces can be five to six orders of magnitude stronger than the Raman signal from the same molecules in bulk volume.

3.5 EM field enhancement in a self-similar, fractal set of metallic nanoparticles. The analysis presented above considers mono-dimensional chains of silver nanoparticles, in which the sole variable describing those networks is the degree of disorder δ. It instead disregards the fractal nature of an aggregate. Here, the optical response of a complex numerical fractal set of metallic nanoparticles (**Fig.7a**) is analyzed as a function of the angle of polarization and the wavelength of the incident EM radiation, in comparison to a simple mono-dimensional chain of particles. The numerical fractal set in **Fig.7a** mimics the dendritic nature of electroless nanoparticles aggregates (**Fig.2e** and images in the **Supporting Information file #2**). It was generated by a stochastic, diffusion limited aggregation (DLA) algorithm where particles, undergoing a random walk due to Brownian motion, cluster together to form aggregates of such particles, revealing a fractal motif [40,84, 85]. A pair correlation analysis[40] (**Fig.7b**) was then applied to the numerical set to derive the effective fractal dimensionality D_f of the aggregate that, for the present configuration, reads as D_f=1.65. Unlike topological dimensions, the fractal index can take non integer values, indicating that a set fills its space qualitatively and quantitatively differently than an ordinary geometrical set does. In this case, a value of D_f of 1.65 indicates that those aggregates are far more complex than a mono-dimensional chain (that is, a line), being distributed in the plane as to resemble a 1 to 2 dimensional manifold. In comparison, the Sierpinski triangle has a fractal dimension of 1.585[50]. The contour plot of the EM enhancement over the domain of interest is reported in **Fig.7c** for a particular configuration (angle of polarization φ=0, λ=510 nm).

Nanoscale

Dynamic Article Links ►

Cite this: DOI: 10.1039/c0xx00000x

www.rsc.org/nanoscale

PAPER

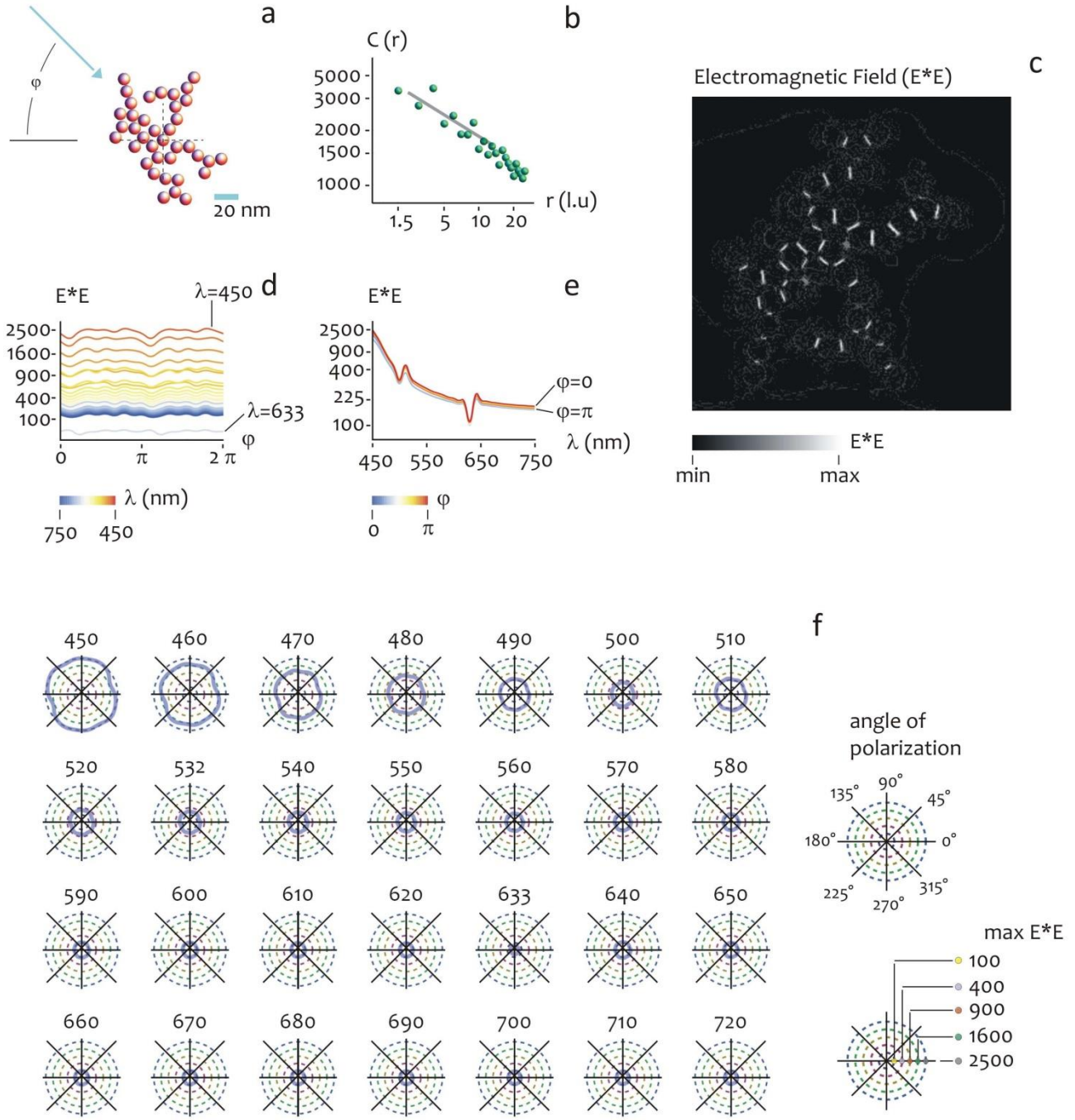

Fig. 7 a numerical diffusion limited fractal aggregate of silver nanoparticles (**a**). Pair correlation density function of the numerical data set, from which the fractal dimension of the aggregate is derived as Df~1.65 (**b**). Contour plot of the EM field intensity generated by the aggregate for a constant angle of polarization (φ=0, λ=510 nm) (**c**). The enhancement of the local electric field is reported as a function of the angle of polarization φ and of the wavelength λ of the incident radiation The observed enhancement of the electric field varies with λ to a large extent, while it shows a low sensitivity to φ (**d**, **e**). The maximum enhancement of the local electric field in the fractal set is reported in a polar form as a function of the angle of polarization φ, for λ varying from 450 to 720 nm (**f**).

In this case, the intensity of the EM field is normalized to one. Optically excited, such a nano-lens develops the nanofocus in the gaps between the nano-spheres, where the local fields are enhanced due to the multiplicative cascade effect of its geometry. This is somehow similar to the response of the self-similar chains of metal nano-spheres described by Li et al. [86], where a finite regular set of spheres, in which the diameter and the distance of the spheres stand in a precise ratio, is theoretically investigated. A random fractal set is axiomatically a self-similar system, that is, a system that preserves its morphology over multiple scales. The fractal dimension measures the degree of such self-similarity.

In **Fig.7d**, the maximum local electric field $|\mathbf{E}|^2$ in the fractal set is reported as a function of the angle of polarization φ, for different wavelengths λ. In this run, the maximum field intensity shows a low sensitivity to φ, with no preferential directions of orientation, therefore, the effect of the angle of polarization on the electric field may be neglected, and this is consistent with the random, disordered nature of the aggregate. Differently from this, the effect of the wavelength λ cannot be disregarded. In **Figure 7e**, The local field shows a very high sensitivity to λ, with values of $|\mathbf{E}|^2$ ranging from 2500, for λ=450 nm, to nearly 100, for λ=750 nm. The EM increment is significant in the low wavelength limit, that is for λ<510 nm, while it rapidly decreases for increasing λ.

In **Fig.7f**, the maximum enhancement of the local electric field in the fractal set is reported in a polar form as a function of the angle of polarization φ, for λ varying from 450 to 720 nm. Notice, in this series, a strong isotropy emerging in the system: here the EM increment resembles the form of a circle. This circular shape and the symmetry of the system is maintained for increasing wavelength, where instead the diameter of the circle, that is the EM intensity, progressively extinguishes in the long wavelength limit. On observing the diagrams in **Fig.7f** in a sequence, the evolution of the EM field takes the form of a monotonous contraction. For this particular fractal set, the spectral maximum of the enhancement is in the blue region, with $|\mathbf{E}|^2$ enhancements that are comprised between 3 and 4 orders of magnitude. Considering that the Raman enhancement is proportional to the fourth power of the local electric field, the cited field should exceed the considerable values of 10^6 to 10^8 in the Raman active centers. These results are consistent with the findings of some classical and very well-known works on surface enhanced Raman Spectroscopy, including [87, 88]. Single silver nano-spheres, or even mono dimensional chains of silver, provide smaller field enhancement. These findings suggest that, for efficient SERS analysis, the active sites of the Raman scattering must be a collective of many, or at least several, nanoparticles, with a random fractal nature.

4 Conclusions

The limitations of current nanotechnology approaches in diagnosis, including silicon chips coated with a meso-porous film, can be surpassed introducing an increasing degree of complexity into the geometry of the devices. Here, on micro-pattering meso-porous silicon films, we obtained hierarchical structures with details at different scales. Those extra not-continuous scales would provide the device with additional functions, including the capability of manipulating biological solutions. Moreover, using an innovative site selective electroless deposition method, we introduced clusters of metal nano-particles into the meso-porous silicon matrix. The major advance of this device is its capability of combining different structures and functions that arise because of its hierarchal small scales. These functions are: (**i**) the capability of manipulating diluted solutions and harvesting small molecules from those solutions (for which the meso-porous silicon substrate is responsible) and (**ii**) the ability of amplifying the electromagnetic field by several orders of magnitude for unique Raman measurements (for which the silver nano-particles networks are responsible). Using this scheme, we realized the size-exclusion-based, elective capture and enrichment of Rhodamine molecules starting from a ultra-low diluted binary solution.

This *proof of principle* verifies that the described method has the potentials of being used for a variety of applications of biomedical interest, including the diagnosis of diseases starting from serum, other biological fluids, or any sample obtained through minimally or non-invasive techniques; and the monitoring and control of the ongoing physiological conditions of individuals.

Acknowledgements

This work has been partially funded from the EU Commission, the European Social Fund and the Calabria Region (POR Calabria FSE 2007-2013), from the Italian Minister of Health under the project “Cancer biomarker detection using micro-structured/super-hydrophobic surfaces and advanced spectroscopy techniques” (Project n. GR-2010-2320665), and from the Cariplo Foundation under the project “New Frontiers in Plasmonic Nanosensing” (Grant no. 2011-0338).

Notes and references

1. P. Aussillous and D. Quéré, *Nature*, 2001, **411**, 924-927.
2. R. Blossey, *Nat. Mater.*, 2003, **2**, 301-306.
3. A. Lafuma and D. Quéré, *Nat. Mater.*, 2003, **2**, 457-460.
4. E. Ueda and P. A. Levkin, *Adv. Mater.*, 2013, **25**, 1234–1247.
5. X. Zhang, F. Shi, J. Niu, Y. Jiang and Z. Wang, *J. Mater. Chem.*, 2008, **18**, 621-633.
6. Y.-L. Zhang, H. Xia, E. Kim and H.-B. Sun, *Soft Matter*, 2012, **8**, 11217-11231.
7. F. De Angelis, F. Gentile, F. Mecarini, G. Das, M. Moretti, P. Candeloro, M. Coluccio, G. Cojoc, A. Accardo, C. Liberale, R. Zaccaria, G. Perozziello, L. Tirinato, A. Toma, G. Cuda, R. Cingolani and E. Di Fabrizio, *Nat. Photonics*, 2011, **5**, 682.
8. A. Accardo, F. Gentile, F. Mecarini, F. De Angelis, M. Burghamme, E. Di Fabrizio and C. Riekel, *Langmuir*, 2010, **26**, 15057–15064.
9. Y. C. Jung and B. Bhushan, *Nanotechnology*, 2006, **17**, 4970.
10. F. Gentile, G. Das, M. Coluccio, F. Mecarini, A. Accardo, L. Tirinato, R. Tallerico, G. Cojoc, C. Liberale, P. Candeloro, P.

Decuzzi, F. De Angelis and E. Di Fabrizio, *Microelectron. Eng.*, 2010, **87** 798-801.
11. F. Gentile, A. Accardo, M. Coluccio, M. Asande, G. Cojoc, F. Mecarini, G. Das, C. Liberale, F. De Angelis, P. Candeloro, P. Decuzzi and E. Di Fabrizio, *Microelectron. Eng.*, 2011, **88** 1749-1752.
12. F. Gentile, E. Battista, A. Accardo, M. Coluccio, M. Asande, G. Perozziello, G. Das, C. Liberale, F. De Angelis, P. Candeloro, P. Decuzzi and E. Di Fabrizio, *Microelectron. Eng.*, 2011, **88**, 2537-2540.
13. M. Nosonovsky and B. Bhushan, *Ultramicroscopy*, 2007, **107** 969–979.
14. M. Nosonovsky and B. Bhushan, *Nano Lett.*, 2007, **7**, 2633–2637.
15. N. Patankar, *Langmuir*, 2004, **20**, 8209–8213.
16. A. Cassie and S. Baxter, *Trans. Faraday Soc.*, 1944, **40**, 546-551.
17. R. Wenzel, *Ind. Eng. Chem.*, 1936, **28**, 988-994.
18. H. Kusumaatmaja, M. Blow, A. Dupuis and J. Yeomans, *Europhys. Lett.*, 2008, **81**, 36003.
19. G. McHale, S. Aqil, N. Shirtcliffe, M. Newton and H. Erbil, *Langmuir* 2005, **21**, 11053-11060.
20. S. Moulinet and D. Bartolo, *Eur. Phys. J. E*, 2007, **24**, 251-260.
21. M. Reyssat, J. M. Yeomans and D. Quéré, *Europhys. Lett.*, 2008, **81**, 26006
22. F. Gentile, M. Coluccio, N. Coppedè, F. Mecarini, G. Das, C. Liberale, L. Tirinato, M. Leoncini, G. Perozziello, P. Candeloro, F. De Angelis and E. Di Fabrizio, *ACS Appl. Mater. Inter.*, 2012, **4**, 3213–3224.
23. M. J. Hancock, J. He, J. F. Mano and A. Khademhosseini, *Small*, 2011 **7**.
24. X. Liu, Q. Wang, J. Qin and B. Lin, *Lab Chip*, 2009, **9**, 1200-1205.
25. C. Wang, T. Yao, J. Wu, C. Ma, Z. Fan, Z. Wang, Y. Cheng, Q. Lin and B. Yang, *ACS Appl. Mater. Inter.*, 2009, **1**, 2613–2617.
26. J. Genzera and K. Efimenkoa, *Biofouling*, 2006, **22**, 339-360.
27. A. L. Hook, N. H. Voelcker and H. Thissen, *Acta Biomater.*, 2009, **5**.
28. K. Na, J. Jung, B. Shin and J. Hyun, *Langmuir*, 2006, **22**, 10889-10892.
29. T. Pauloehrl, G. Delaittre, M. Bruns, M. Meisler, H. G. Borner, M. Bastmeyer and C. Barner-Kowollik, *Angew. Chem. Int. Edit.*, 2012, **51**, 9181–9184.
30. T. Limongi, F. Cesca, F. Gentile, R. Marotta, R. Ruffilli, A. Barberis, M. D. Maschio, E. M. Petrini, S. Santoriello, F. Benfenati and E. Di Fabrizio, *Small*, 2013, **9**, 402–412.
31. F. Gentile, M. Moretti, T. Limongi, A. Falqui, G. Bertoni, A. Scarpellini, S. Santoriello, L. Maragliano, R. P. Zaccaria and E. Di Fabrizio, *Nano Lett.*, 2012, **12**, 6453−6458.
32. T. Ishizaki, N. Saito and O. Takai, *Langmuir*, 2010, **26**, 8147–8154.
33. F. L. Geyer, E. Ueda, U. Liebel, N. Grau and P. A. Levkin, *Angew. Chem. Int. Edit.*, 2011, **50**, 8424–8427.
34. G. McHale, N. Shirtcliffe and M. Newton, *Analyst, 129, 2004*, 2005, 129.
35. G. Whitesides, *Nat. Biotechnol.*, 2003, **21**, 1161.
36. P. E. Sheehan and L. J. Whitman, *Nano Lett.*, 2005, **4**, 803–807.
37. J. Zhu, S. K. Ozdemir and L. Yang, *Nat. Photonics*, 2011, **5**, 653-654.
38. D. Lis, Y. Caudano, M. Henry, S. Demoustier-Champagne, E. Ferain and F. Cecchet, *Adv. Optical Mater.*, 2013, **1**, 244–255.
39. M. L. Coluccio, G. Das, F. Mecarini, F. Gentile, A. Pujia, L. Bava, R. Tallerico, P. Candeloro, C. Liberale, F. De Angelis and E. Di Fabrizio, *Microelectron. Eng.*, 2009, **86**, 1085-1088.
40. F. Gentile, M. Coluccio, A. Toma, E. Rondanina, M. Leoncini, F. De Angelis, G. Das, C. Dorigoni, P. Candeloro and E. Di Fabrizio, *Microelectron. Eng.*, 2012, **98**, 359-362.
41. L. A. Liotta, M. Ferrari and E. Petricoin, *Nature*, 2003, **425**, 905.
42. E. F. Petricoin and L. A. Liotta, *Curr. Opin. Biotech.*, 2004, **15**, 24–30.
43. H. Foll, M. Christophersen, J. Carstensen and G. Hasse, *Mater. Sci. Eng.*, 2002, **39**, 93–141.
44. F. Gentile, R. L. Rocca, G. Marinaro, A. Nicastri, A. Toma, F. Paonessa, G. Cojoc, C. Liberale, F. Benfenati, E. Di Fabrizio and P. Decuzzi, *ACS Appl. Mater. Int.*, 2012, **4**, 2903–2911.
45. J. Bisquert, G. Garcia-Belmonte and F. Fabregat-Santiago, *J. Solid State Electrochem.*, 1999, **3**, 337-347.
46. M. L. Coluccio, F. Gentile, M. Francardi, G. Perozziello, N. Malara, P. Candeloro and E. Di Fabrizio, *Sensors*, 2014, **14**, 6056-6083.
47. C. J. Russo and J. A. Golovchenko, *P. Natl. Acad. Sci. USA*, 2012, **109**, 5953–5957.
48. A. A. Stekolnikov, J. Furthmuller and F. Bechstedt, *Phys. Rev. B*, 2002, **65**, 115318.
49. F. Gentile, M. L. Coluccio, P. Candeloro, M. Barberio, G. Perozziello, M. Francardi and E. Di Fabrizio, *J. Vac. Sci. Technol. B*, 2014, **32**, 031804/031801-031812.
50. J. Feder, *Fractals*, Plenum Press, New York, 1988.
51. F. Gentile, L. Tirinato, E. Battista, F. Causa, C. Liberale, E. Di Fabrizio and P. Decuzzi, *Biomaterials*, 2010, **31**, 7205-7212.
52. S. Godefroo, M. Hayne, M. Jivanescu, A. Stesmans, M. Zacharias, O. I. Lebedev, G. V. Tendeloo and V. V. Moschalkov, *Nat. Nanotechnol.*, 2008, **3**, 174-178.
53. M. Fasano, S. Curry, E. Terreno, M. Galliano, G. Fanali, P. Narciso, S. Notari and P. Ascenzi, *IUBMB Life*, 2005, **57**, 787–796.
54. P. A. Zunszain, J. Ghuman, T. Komatsu, E. Tsuchida and Stephen Curry, *BMC Struct. Biol.*, 2003, **3**, 1-9.
55. U. Kragh-Hansen, F. Hellec, B. de Foresta, M. le Maire and J. V. Møller, *Biophys. J.*, 2001, **80**, 2898–2911.
56. H.-H. Cai, X. Zhong, P.-H. Yang, W. Wei, J. Chen and J. Cai, *Colloids and Surfaces A: Physicochem. Eng. Aspects*, 2010, **372**, 35–40.
57. A. Garro, D. Beltramo, R. Alasino, V. Leonhard, V. Heredia and I. Bianco, *Int. J. Nanomed.*, 2011, **6**, 1193–1200.
58. M. Hawkins, P. Soon-Shiong and N. Desai, *Adv. Drug. Deliv. Rev.*, 2008, **60**, 876–885.
59. S. Sebak, M. Mirzaei, M. Malhotra, A. Kulamarva and S. Prakash, *Int. J. Nanomed.*, 2012, **5**, 525–532.
60. D. Zhong, A. Douhal and A. H. Zewail, *P. Natl. Acad. Sci. USA*, 2000, **97**, 14056–14061.
61. P. E. Sheehan and L. J. Whitman, *Nano Lett.*, 2005, **5**, 803–807.

62. W. G. Lewis, Z. Shen, M. G. Finn and G. Siuzdak, *Int. J. Mass Spectrom.*, 2003, **226**, 107–116.
63. J. Wei, J. M. Buriak and G. Siuzdak, *Nature*, 1999, **399**, 243-246.
64. H. H. P. Yiu and P. A. Wright, *J. Mater. Chem.*, 2005, **15**, 3690–3700.
65. O. Sel, S. Sallard, T. Brezesinski, J. Rathousky, D. R. Dunphy, A. Collord and B. M. Smarsly, *Adv. Funct. Mater.*, 2007, **17**, 3241–3250.
66. J. S. Ananta, B. Godin, R. Sethi, L. Moriggi, X. Liu, R. E. Serda, R. Krishnamurthy, R. Muthupillai, B. R. D, L. Helm, M. Ferrari, L. J. Wilson and P. Decuzzi, *Nat. Nanotechnol.*, 2010, **5**, 815-821.
67. P. Decuzzi, F. Gentile, A. Granaldi, A. Curcio, F. Causa, C. Indolfi, P. Netti and F. M, *Int. J. Nanomed.*, 2007, **2**, 689–696.
68. M. Gaspari, M. M.-C. Cheng, R. Terracciano, X. Liu, J. Nijdam, L. Vaccari, E. Di Fabrizio, E. F. Petricoin, L. A. Liotta, G. Cuda, S. Venuta and M. Ferrari, *J. Proteome Res.*, 2006, **5**, 1261-1266.
69. Y. Hu, A. Bouamrani, E. Tasciotti, L. Li, X. Liu and M. Ferrari, *ACS Nano*, 2010, **4**, 439–451.
70. R. Terracciano, M. Gaspari, F. Testa, L. Pasqua, P. Tagliaferri, M. M.-C. Cheng, J. Nijdam, E. F. Petricoin, L. A. Liotta, G. Cuda, M. Ferrari and S. Venuta, *Proteomics*, 2006, **6**, 3243-3250.
71. H. Gelderblom, O. Bloemen and J. H. Snoeijer, *J. Fluid Mech.*, 2012, **709**, 69-84.
72. H. Masoud and J. D. Felske, *Phys. Fluids*, 2009, **21**, 042102.
73. Y. Astier, L. Data, R. P. Carney, F. Stellacci, F. Gentile and E. Di Fabrizio, *Small*, 2010, **7**, 455-459.
74. P.-H. Lee, V. Helms and T. Geyer, *J. Chem. Phys.*, 2012, **137**, 145105.
75. E. C. Yusko, J. M. Johnson, S. Majd, P. Prangkio, R. C. Rollings, J. Li, J. Yang and M. Mayer, *Nat. Nanotechnol.*, 2011, **6**, 253-260.
76. M.-m. Kim and A. L. Zydney, *J. Colloid Interf. Sci.*, 2004, **269**, 425–431.
77. R. D. Deegan, O. Bakajin, T. F. Dupont, G. Huber, S. R. Nagel and T. A. Witten, *Nature*, 1997, **389**, 827-829.
78. T. Qiu and P. Chu, *Mat. Sci. Eng. R*, 2008, **61**, 59–77.
79. T. Qiu, X. Wu, Y. Mei, P. Chu and G. Siu, *Appl. Phys. A-Mater.*, 2005, **81**, 669–671.
80. A. R. Tao, S. Habas and P. Yang, *Small*, 2008, **4**, 310 – 325.
81. R. Esteban, R. W. Taylor, J. J. Baumberg and J. Aizpurua, *Langmuir*, 2012, **28**, 8881−8890.
82. H.-H. Wang, C.-Y. Liu, S.-B. Wu, N.-W. Liu, C.-Y. Peng, T.-H. Chan, C.-F. Hsu, J.-K. Wang and Y.-L. Wang, *Adv. Mater.*, 2006, **18**, 491–495.
83. G. Das, F. Mecarini, F. Gentile, P. Candeloro, C. Liberale, F. De Angelis, H. Kumar, G. Cuda and E. Di Fabrizio, *BioSens. BioElectron.*, 2009, **24**, 1693–1699.
84. T. Witten and L. Sander, *Phys. Rev. Lett.*, 1981, **47**, 1400-1403.
85. Z. Zhang and M. Lagally, *Science*, 1997, **276**, 377-383.
86. K. Li, M. Stockman and D. Bergman, *Phys. Rev. Lett.*, 2003, **91**, 227402.
87. K. Kneipp, Y. Wang, H. Kneipp, L. T. Perelman, I. Itzkan, R. R. Dasari and M. S. Feld, *Phys. Rev. Lett.*, 1997, **78**, 1667–1670.
88. S. Nie and S. R. Emory, *Science*, 1997, **275**, 1102-1106.